Number 2, Volume XIX, July 2019

INVESTIGATION OF THE CRACK DRIVING FORCE IN WHEEL-RAIL CONTACT

Michal Kráčalík[1]

Summary: This paper investigates the crack driving force in the wheel-rail contact using a finite element model. The presented work determines significant model variables such as an effect of the loading type, friction coefficients, cyclic plasticity and the number of the integration contour on the crack driving force and lays the foundation for the further development of the model and computational schemes.

Key words: wheel-rail contact, crack, crack driving force, finite element model

INTRODUCTION

Surface cracks are presents in the wheels and the rails due to their mutual contact (1-2). The initial contact conditions are changed during the rolling/sliding contact (2-3), and the contact geometry is slowly changed by the plastic deformation and wear (4). Wear is thought to be the product of the heavily plastic deformation near the contact surface that is mainly influenced by the surface roughness (5). The temperature effects can affect the wear and cracks in the wheel and in the rail (6-11).

Finite element (FE) simulations are widely used to investigate surface cracks in the wheel-rail contact for many years (12-13). The contact loading is usually prescribed as the moving Hertz pressure distribution (14-21) or it is applied by the modelled wheel (13, 22-25). Usually 2-D FE models with linear-elastic (14, 15, 17, 18, 19, 21, 22, 24,25) or elastic-plastic material behaviour (14-19) are employed. The 3-D FE models are used mostly with linear-elastic material properties (26-28). The stress intensity factor and the configurational (also called material) forces represent mostly the crack driving force (14-18, 20, 21, 29).

The aim of the work is to determine the most significant model variables that will be used as a foundation for the further development of the model and computational schemes. The focus is on the crack driving force in context of cyclic plasticity occurred in the wheel-rail contact. The temperature effects are not included in the presented paper and the crack is located into the rail.

The most work was done as part of the PhD. thesis (30). Unless stated differently, the figures are directly taken from (30) without further reference.

---

[1] Dr. Michal Kráčalík, Untere Haupstraße 48/5, 2424 Zurndorf, Austria, Tel.: +43 664 7505 0660, E-mail: michal.kracalik@gmail.com

1. CRACK DRIVING FORCE

1.1 Configurational force concept

The configurational force (also known as material force) concept can handle with un-proportional cyclic loading, elastic-plastic material description and is chosen as a crack driving force; more details can be found for instance in (31).

The basic theory and the numerical implementation of the configurational force concept were presented in the papers (25, 29) and will be reproduced in subchapters 1.2 and 1.3.

1.2 Definition of the configurational force concept

The configurational body force for linear-elastic material properties follow the description in the papers (32-33) and it is designated as the vector

$$\underline{f} = -\nabla \cdot \underline{\underline{C}}, \qquad (1)$$

where $\underline{\underline{C}}$ is the configurational stress tensor expressed as

$$\underline{\underline{C}} = \phi \underline{\underline{I}} - \underline{\underline{F}}^T \underline{\underline{S}} \qquad (2)$$

with $\underline{\underline{I}}$ as the unit tensor, ϕ as the strain energy density, $\underline{\underline{F}}$ as the deformation gradient tensor and $\underline{\underline{S}}$ as the first Piola-Kirchhoff stress tensor.

$\underline{\underline{F}}$ is calculated by the displacement gradient $\nabla \underline{u}$ as

$$\underline{\underline{F}} = \underline{\underline{I}} + \nabla \underline{u}, \qquad (3)$$

where displacement gradient $\nabla \underline{u}$ is expressed as $\nabla \underline{u} = \frac{\partial \underline{u}}{\partial \underline{X}}$; $\underline{u}$ is the displacement and $\underline{X}$ is the position in the original configuration.

In a FEM software can be $\underline{\underline{S}}$ calculated from the Cauchy stress $\underline{\underline{T}}$ as

$$\underline{\underline{S}} = \det \underline{\underline{F}}\, \underline{\underline{T}}\, \underline{\underline{F}}^{-T}. \qquad (4)$$

For plastic material properties $\underline{f}$ is designated as (34)

$$\underline{f}_{pl} = -\nabla(\phi_{el} \underline{\underline{I}} - \nabla \underline{u}^T \underline{\underline{S}}), \qquad (5)$$

where ϕ_{el} is the elastic part of the strain energy density. It is the available energy to support crack growth while the plastic part of strain energy density ϕ_{pl} is used for the plastic deformation. The whole strain energy density is defined simply as (25):

$$\phi = \phi_{pl} + \phi_{el}. \qquad (6)$$

Using ϕ instead of ϕ_{el} in equation (5) would give result identical with J-integral (25) that is not suitable measure for crack driving force in the rolling/sliding contact applications requiring usage of the incremental theory of plasticity (29).

1.3 Numerical implementation of the configurational force concept

The configurational force vector can be computed on the nodes of a finite element by equation (7) as (35-36):

$$\underline{g}_i^I = \int_{V_e} \underline{\underline{N}}^I \, \underline{f} \, dV = \int_{V_e} \underline{\underline{N}}^I_{,\underline{X}_j} \, \underline{\underline{C}}_{ij} \, dV \qquad (7)$$

where $\underline{g}_i^I$ is the configurational force component at node I by integrating the configurational body force $\underline{f}$ on the element e and $\underline{\underline{N}}^I$ is the matrix containing the shape functions corresponding to the node I ; $\underline{\underline{N}}^I_{,X_j}$ is the gradient matrix (35-36).

The total configurational force at a node *k* is $\underline{g}_i^I$ collected from all elements surrounding the node *k*.

$$\underline{g}_i^k = \sum_e \underline{g}_i^I \, . \qquad (8)$$

The deformation gradient $\underline{\underline{F}}$ is computed by the element shape functions $\underline{\underline{N}}^I$. The displacement $\underline{u}$ at the nodes $\underline{u}^I$ and its gradient $\underline{u}_{,X_j}$ are defined as:

$$\underline{u} = \underline{\underline{N}}^I \underline{u}^I \text{ and} \qquad (9)$$

$$\underline{u}_{,X_j} = \underline{\underline{N}}^I_{,X_j} \underline{u}^I \, . \qquad (10)$$

2. TYPE OF THE APPLIED CONTACT LOADING

The two contact loadings are compared - the moving Hertz pressure distribution and the loading applied through the wheel part loaded by a prescribed load.

Fig. 1 shows the comparison between two modelled types of the applied loading in the 2-D plane strain FE Model. The blue curve represents contact forces prescribed by a Hertz pressure distribution on the rail surface. The red lines represent calculated contact forces on the nodes of the meshed rail surface produced by the loaded wheel. The contact forces between the crack faces of the embedded surface crack can be seen as red lines parallel to the rail surface in Fig. 1. Here, a linear-elastic material description is used in the investigation and the full slip is assumed (see description of the Fig. 1 for more details).

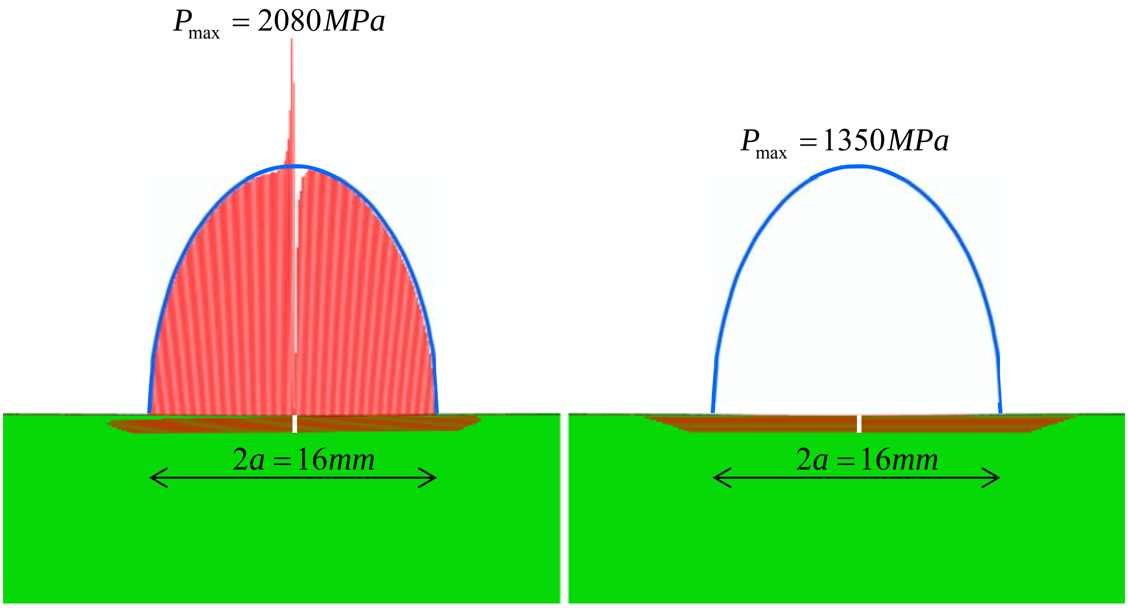

a) b)

Fig. 1 - The comparison between distributions of the contact forces produced by the loaded wheel a) and by the surface forces prescribed by a moving Hertz pressure distribution b) on the rail surface and between the crack faces. The loaded wheel interacts with the embedded surface crack and produces a fluctuation of the forces near the crack normal to the contact surface. The surface crack is marked by a white horizontal line in the rail below the center of the contact patch. The loaded wheel (a) and the Hertz pressure (b) are running from left to right in an acceleration mode with longitudinal slip of 2 % representing a full slip case. Accordingly the traction orientation in the rail shows opposite to the running direction from right to left. The maximum contact pressure is set to Pmax = 1350 MPa in the Hertz case and the longitudinal contact patch size is for both cases 2a = 16 mm. A peak of Pmax = 2080 MPa is visible in the FE model with the loaded wheel (a) as a result of the interaction of the crack with the contacting wheel.

Fig. 2 shows the crack driving force originating from the crack tip over the relative rolling time. Mode I is according to the fracture mechanics an opening mode (the crack grows parallel to the crack) and Mode II is a shear mode.

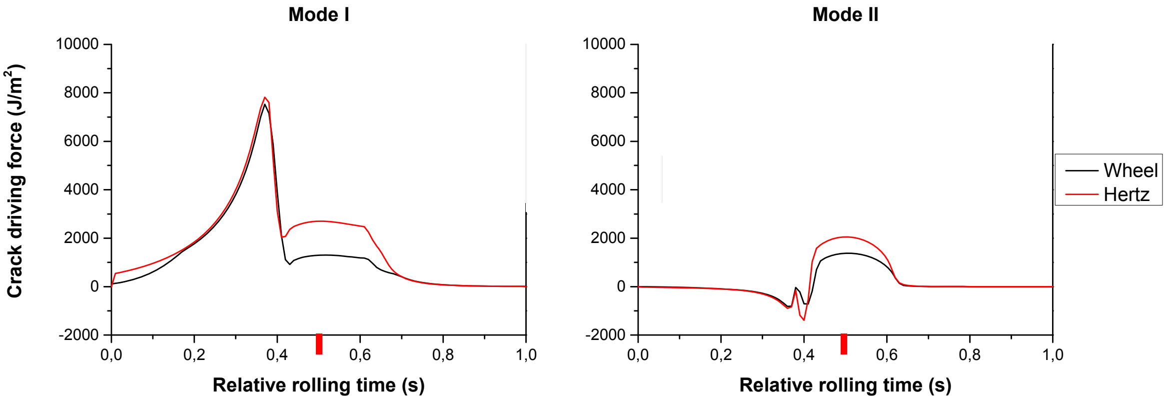

a) b)

Fig. 2 - The crack driving forces originating from the crack tip are plotted for a FE model with the loaded wheel and for a FE model loaded by a Hertz pressure and traction forces over the relative rolling time for a) Mode I and b) Mode II b). A wheel load and a maximum contact pressure of 1350 MPa are prescribed as well as a longitudinal slip of 2 % which represents a full slip case. The 1 mm deep surface crack is modelled normal to the contact surface. The friction between the crack faces is assumed as 0.5. The material is modelled with linear-elastic properties. Differences in the computed crack driving forces are calculated just when the wheel interacts with the crack at a relative rolling time of 0,37 – 0,63 s.

The computing time is compared between the two models. The total computation time is approximately three times longer for the FE model loaded by the wheel than for the Hertz model using linear-elastic material properties, see Table 1.

Tab 1: Comparison of the computation time of the two FE models that use linear-elastic material properties.

FE Model	Loaded by wheel	Hertz
DoF	15750	8976
Abaqus time (1 CPU)	9 min. 57 s	2 min. 1 s.
Configurational force postprocessing time (1 CPU)	35 min. 52 s	13 min. 37 s
Total time	45 min. 49 s	15 min. 38 s

3. 2-D FE CRACK MODEL LOADED BY SURFACE FORCES

The preceding chapter showed numerically efficiency of the 2-D model loaded by the moving Hertz pressure distribution alongside with relatively small differences in the computed crack driving force in comparison with the FE model modelled by the loaded wheel. This chapter describe 2-D FE crack model loaded by surface forces (moving hertz pressure distribution) in more detail. The inclined crack will be modelled instead of the straight crack used in the principal investigation showed in the preceding chapter.

The model is assembled of a rectangle (rail) with an out-of-plane thickness of 10 mm. Plane strain conditions and thus line contact loading are assumed. The rail part is 300 mm long and has a height of 40 mm. The loading is prescribed as a moving Hertz pressure distribution without (free rolling) and with traction (full slip). The loading applied via forces at the surface nodes move from the left to the right (Hertz pressure distribution). The traction forces are oriented in opposite direction and describe an acceleration mode. The model is plotted in Fig 3a. The system of the applied load is sketched in Figs. 3b, c.

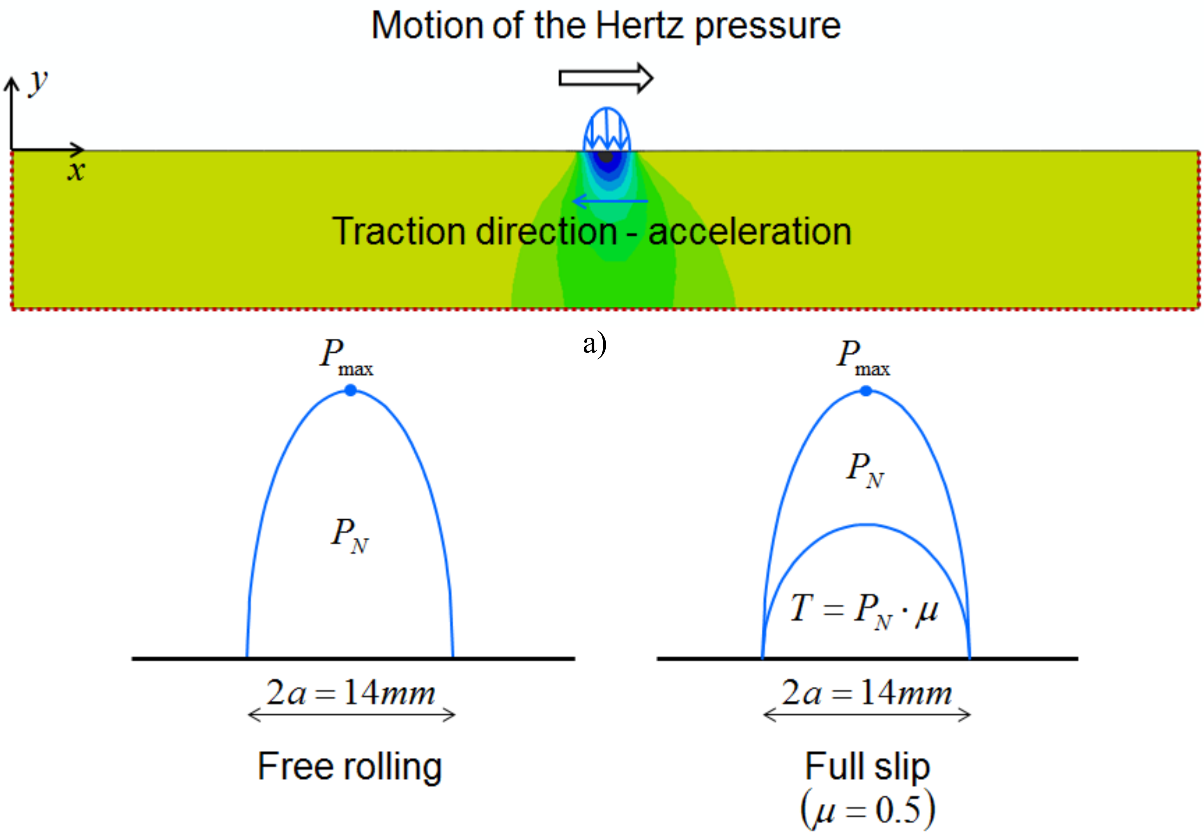

a)

b)

c)

Fig. 3 - Rail part with the applied load (a). The fixed boundary conditions are sketched by a dotted line (a). The contact patch has a longitudinal size 2a = 14mm (b, c). The friction coefficient μ = 0.5.

The inserted crack is oriented with 30° degrees to the rail surface in the middle of the rail. The crack depth is taken with 0.5 mm. The local coordinate system of the crack is plotted in Fig 4.

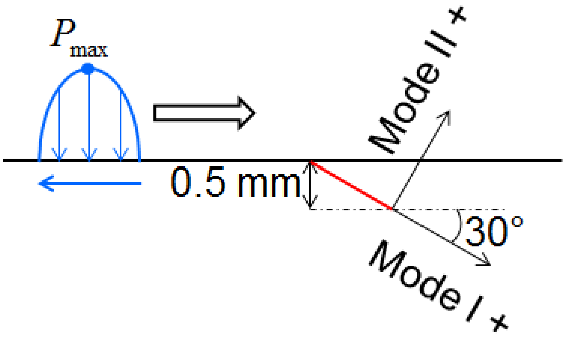

Fig. 4 - The coordinate system of the crack with marked Modes I and II. A plus (+) indicates the positive orientation of the crack driving force.

The material description uses either linear-elastic material properties or an elastic-plastic Chaboche material model. The set of parameters of the Chaboche (combined isotropic-kinematic hardening) material model of rail grade R260 can be found in literature (24).

Basic numerical properties of the FE model are the mesh element size and the vehicle/track parameters as e.g. normal load and friction coefficients. These parameters are investigated in chapters 4.1 – 4.4 using linear-elastic material properties. Chapters 4.5 – 4.6 are devoted to plastic deformation and cyclic loading.

4. NUMERICAL INVESTIGATIONS

4.1 Mesh dependence of the 2-D FE crack model

The used mesh size determines strongly the accuracy of the in crack and contact calculations. Hence, two element sizes around the crack are compared, see Fig. 5a. The crack driving force is computed along several integration contours. The integration contours and mesh element sizes are shown in Figs. 5b, c and the computed crack driving force in the Fig. 6.

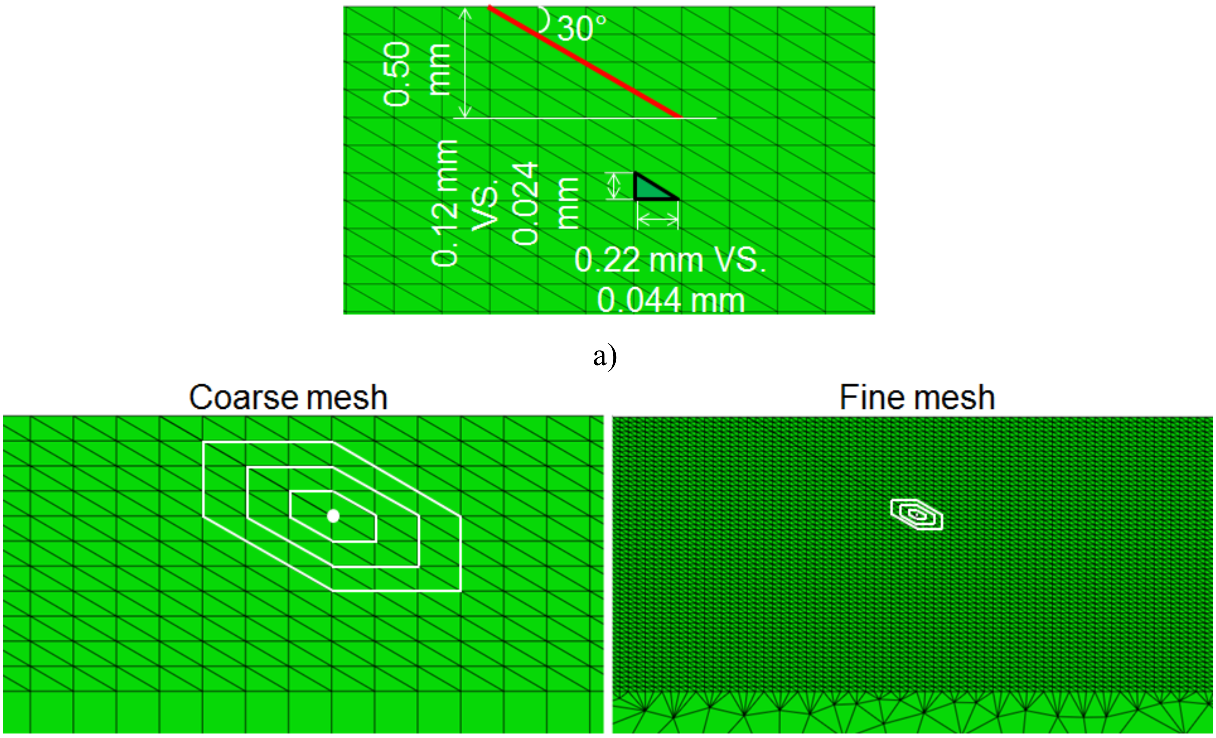

a)

b) c)

Fig. 5 - Geometry of the modelled crack and both mesh element sizes (a). Four integration contours are marked by a white colour for the coarse mesh (b) and the fine mesh (c). The crack tip (1st integration contour) is located in the center of the white area.

The computed crack driving forces are plotted for the two examined element sizes and four integration contours in Fig. 6. They are plotted for Mode I in Figs. 6a, b and for Mode II in Figs. 6c, d; for the coarse mesh in Figs 6a, c and for the fine mesh in Figs. 6b, d. The computed crack driving forces in Mode I are independent from the chosen contours, see Figs. 6a and c. Small numerical discrepancies are visible using a coarse mesh when the crack faces are in contact. The integration contours are path independent for homogenous linear-elastic material properties (34, 37). However, pronounced path dependence is noticeable for Mode II and both mesh element sizes. The path dependencies are visible for Mode II only while the crack faces are pressed together by the contact load and can be seen at a relative rolling time of 0.37 - 0.63 in Figs. 6c, d. Crack driving force Mode II path dependency is reported in wheel/rail contact problems using configurational (material) forces in the literature (18).

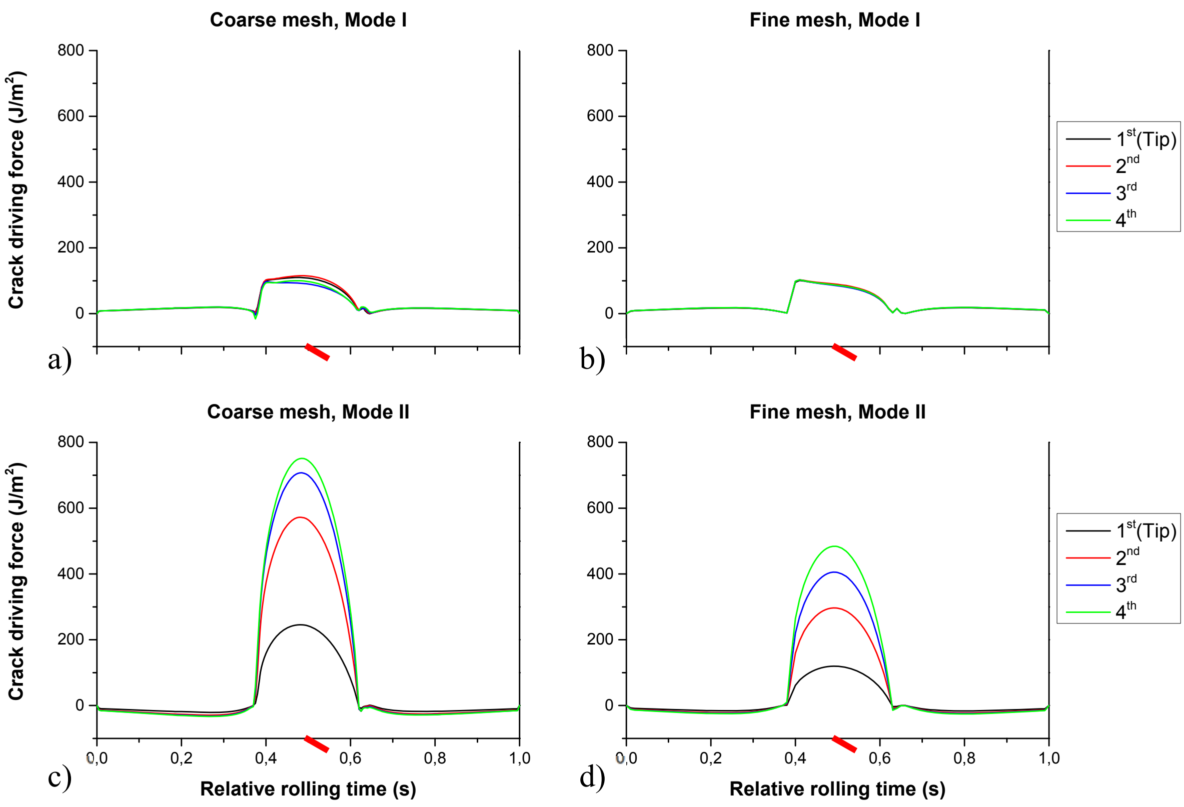

Fig. 6 - The four crack driving force contours are plotted over the relative rolling time for Mode I (a, b) and for Mode II (c, d). The calculated crack driving forces are plotted for coarse mesh (a, c) and for a fine mesh (b, d). A maximum contact pressure of 800 MPa is prescribed in a free rolling case. Frictionless contact is assumed between the crack faces. The model uses linear-elastic material properties. The contour path dependency is visible for Mode II while the crack faces are pressed together at a relative rolling time of 0.37 – 0.63 s, see b, d.

The computing time is compared between the coarse and the fine mesh. The total computation time is approximately 14 times longer for the fine mesh than for the coarse mesh using linear-elastic material properties, see Table 2. The coarse mesh is used in the following investigations.

Tab 2: Comparison of the computing time of the two meshes using linear-elastic material properties. The parameters of the workstation are not listed as long we are interested in the relative difference of the computational time between Coarse and Fine mesh.

Mesh	Coarse mesh	Fine mesh
DoF	2658	27716
Abaqus time (1 CPU)	46 s.	11 min. 35 s.
Configurational force postprocessing time (1 CPU)	4 min. 31 s.	64 min.
Total time	5 min. 17 s.	75 min. 35 s.

4.2 Influence of the contact pressure on the crack driving force

The contact pressure is the main loading parameters in contact applications. The influence of contact pressures on crack driving force is investigated with constant (17), (20) or variable longitudinal contact patch size (16). However, the contact patch size changes in real applications not only due to the contact pressure as a function of the loading but also because of the plastic deformation. The effect of the plastic deformation and cyclic loading are investigated later in chapters 4.5. In this chapter are investigated two load cases with a maximum contact pressure of 800 MPa, see Figs. 7a, c and with 1200 MPa, see Figs. 7b, d. The longitudinal size of the contact patch is taken as 14 mm.

The contact pressure influences the computed crack driving force mainly in the Mode II, see Figs. 7c, d. The computed crack driving forces are negligibly influenced by the contact pressure in Mode I, see Fig. 7a, b. The crack growth for an inclined crack in a free rolling loading case is mainly Mode II dominated.

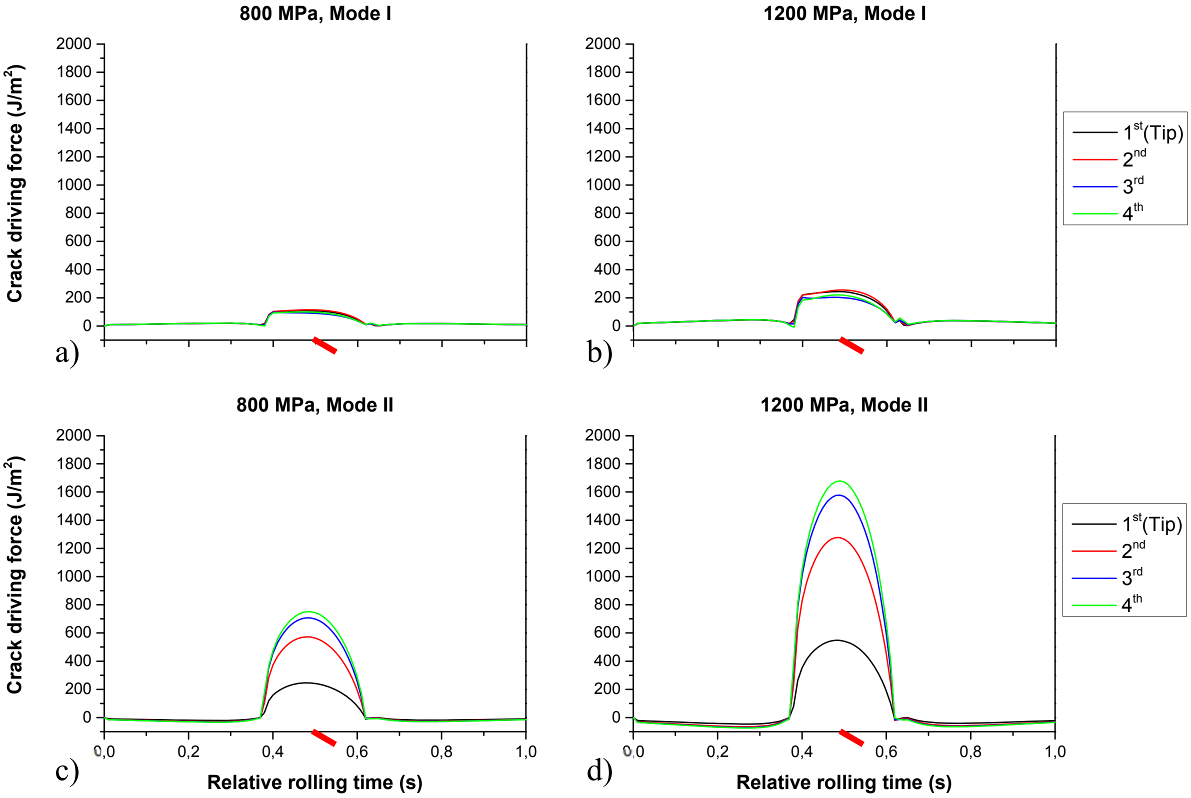

Fig. 7 - Four crack driving force contours are plotted over the relative rolling time for Mode I (a, b) and for Mode II (c, d). The computed crack driving forces are plotted for a maximum contact pressure of 800 MPa (a, c) and for a maximum contact pressure of 1200 MPa (b, d) in a free rolling case. A frictionless contact is assumed between the crack faces. The FE utilizes linear-elastic material properties.

4.3 Influence of the wheel/rail friction on the crack driving force

To see the influence of the wheel/rail friction, two friction coefficients are evaluated: 0.00 (a free rolling case) and 0.50 (in a full slip case). The results are shown for a maximum contact pressure of 800 MPa and frictionless contact between the crack faces in Fig. 8. The impact of the crack faces friction on the crack driving force is evaluated in the next chapter.

The computed crack driving forces are plotted for a free rolling case in Figs. 8a, c and for a full slip case in Figs. 8b, d. The crack driving forces are plotted for Mode I in Figs. 8a, b and for Mode II in Figs. 8c, d. The computed crack driving forces increase significantly for both Modes in a full slip case. Two peaks are calculated in the full slip case.

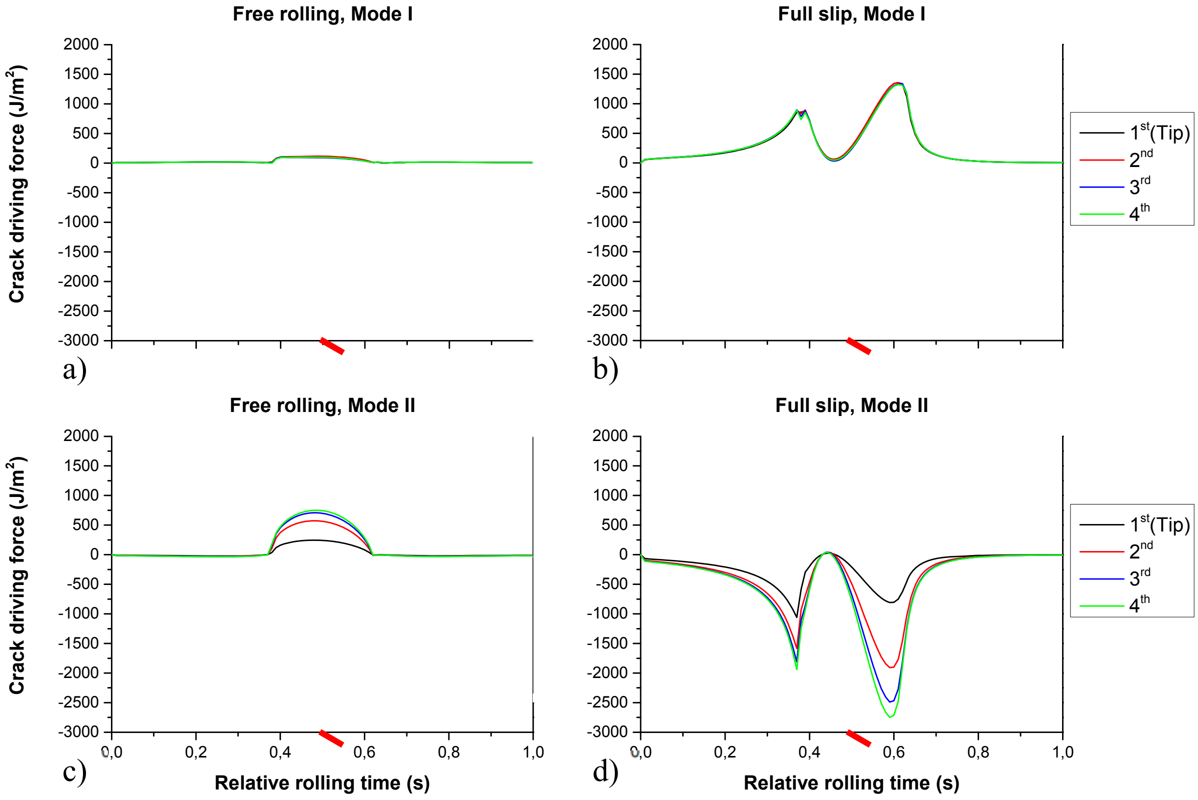

Fig. 8 - The four crack driving force contours are plotted over the relative rolling time for Mode I (a, b) and for Mode II (c, d). The results are plotted for a free rolling case - wheel/rail friction coefficient 0.00 (a, c) and for a full slip case - wheel/rail friction coefficient 0.50 (b, d). The maximum contact pressure is chosen to be 800 MPa. A frictionless contact is assumed between the crack faces. The FE model utilizes linear-elastic material properties.

4.4 Influence of the friction between the crack faces on the crack driving force

Two friction coefficients are evaluated between the crack faces: 0.00 (frictionless) and 0.50 (non-frictionless). The results are plotted for a maximum contact pressure of 800 MPa and a free rolling case in Fig. 9.

The computed crack driving forces are shown for frictionless contact between the crack faces in Figs. 9a, c and friction between crack faces Figs. 9b, d. The computed crack driving forces are significantly reduced for Mode II using a friction coefficient of 0.5 between the crack faces, see Figs. 9b, d. The crack driving forces are practically unaffected by the crack face friction in Mode I, see Figs. 9a, b.

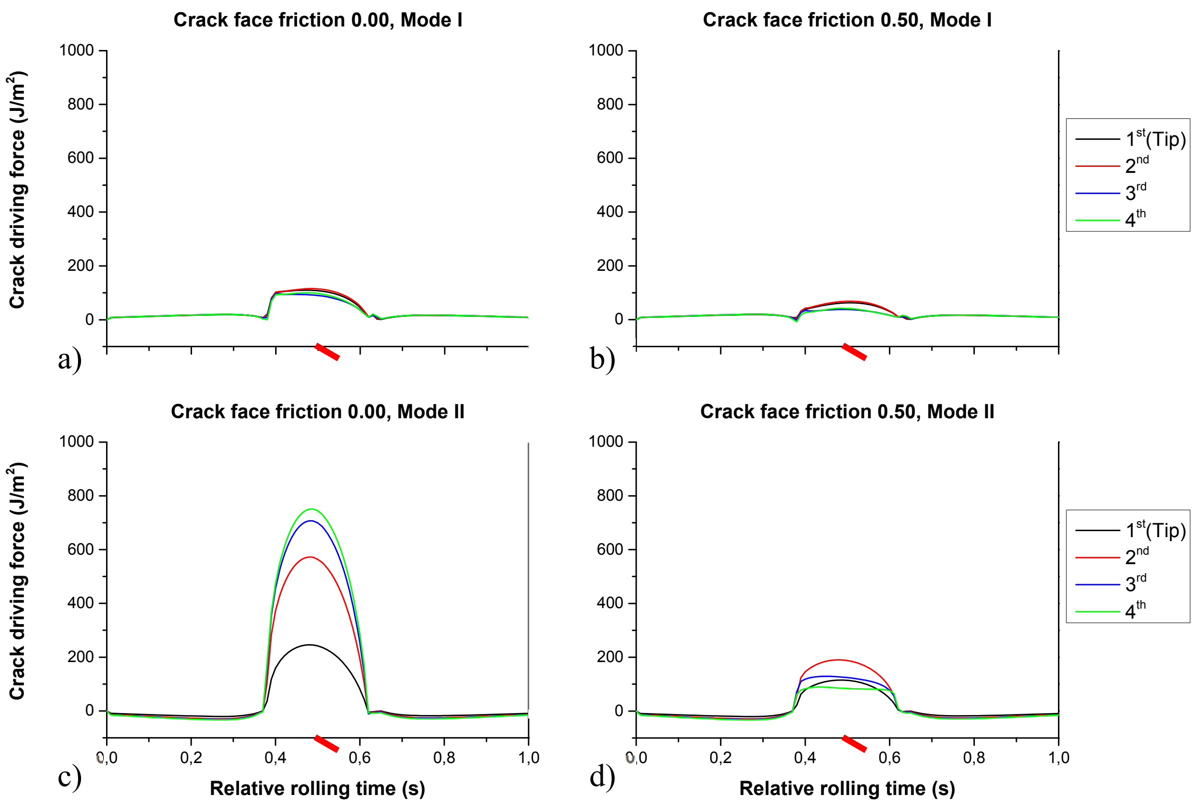

Fig. 9 - The four crack driving force contours are plotted over the relative rolling time for Mode I (a, b) and for Mode II (c, d). The results are plotted for frictionless contact between the crack faces (a, c) and for a friction coefficient 0.5 between the crack faces (b, d). The maximum contact pressure is chosen to be 800 MPa in a free rolling case. The model utilizes linear-elastic material properties. The computed crack driving forces are significantly reduced for Mode II and friction between the crack faces, see Figs. 9c, d.

4.5 The effect of the plastic deformation on the crack driving force

The influence of the material on the crack driving forces is investigated using linear-elastic material properties and elastic-plastic material properties. Fig. 10 shows the effect of the plastic deformation on the computed crack driving force. The results are presented for a full slip case with maximum contact pressure of 800 MPa and a frictionless contact between the crack faces in Mode I. There is no difference in the computed crack driving forces computed for all integration contours between linear-elastic and elastic-plastic material properties if plastic deformation produced by the moving surface load does not reach the integration contours around the crack tip, see Figs. 10a, b at a relative rolling time of 0.30 s. The crack driving forces become contour path dependent when the plastic deformation intersects the integration contours, see Figs. 10b, d at a relative rolling time of 0.40 s; the same conclusion was drawn in (3) and the FE model is supposed to be verified. In more general, the dependency of crack driving force contours on the plastic deformation is reported for incremental plasticity in the literature, see e.g. (32, 38).

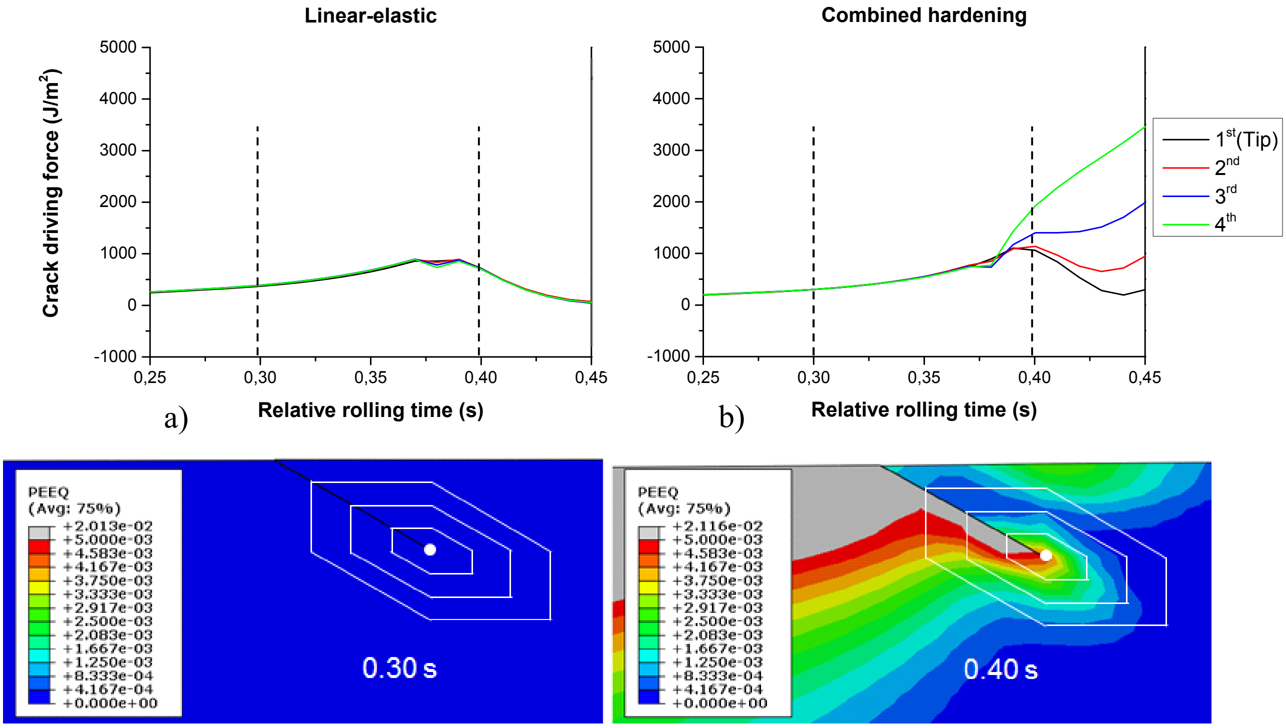

a) b)

c) d)

Fig. 10 - The crack driving force for all four contours is plotted over the relative rolling time for Mode I using linear-elastic material properties (a) and elastic-plastic material properties with combined isotropic-kinematic hardening behaviour (b). The results are plotted for frictionless contact between the crack faces, a maximum contact pressure of 800 MPa is assumed for the full slip case. The crack driving forces are contour independent as long as a plastic deformation produced by the surface loading does not intersect the integration contours at about 0.37 s. The contours are plotted over the plastic deformation at 0.3 s and 0.4 s rolling time see Figs. 10 c, d.

The computed crack driving forces change its magnitude across the integration contour due to the plastic deformation, see Figs. 10b, d. The 4th integration contour encloses the biggest area of the material (contours are counted from the crack tip which is marked by a white dot in Figs. 10c, d). The highest crack driving force is computed for the 4th integration contour. Due to the strong plastic deformation by the surface load the bigger contours produce unrealistically high crack driving forces and on the crack tip contour remains comparable between all regarded cases.

4.6 Cyclic analysis

A cyclic compression/tension single element test with a controlled stress amplitude was conducted using a Chaboche material model of rail grade R260 in order to investigate the ratcheting response of the material model; Fig. 11. The used material parameters are listed in the literature (24).

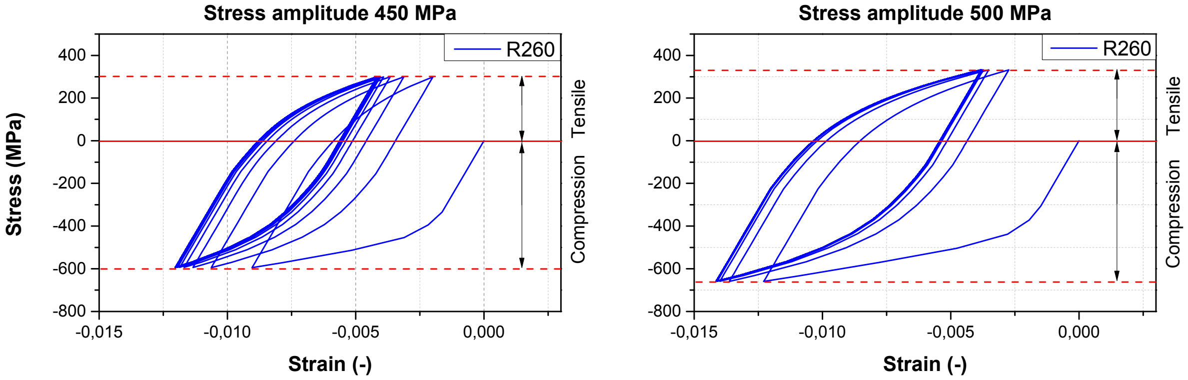

a) b)

Fig. 11: The cyclic compression/tensile single element test with a controlled stress amplitude of 450 MPa (a) and of 500 MPa (b). The stress ratio of the experiment is R= -2 (asymmetric alternating stress). A stabilisation of the ratcheting behaviour (stable hysteresis loop) is reached quickly after four loading cycles with a stress amplitude of 500 MPa (b). Overall one hundred loading cycles were performed.

A stable hysteresis loop is established after a small amount of loading cycles, see Fig. 10. A stable hysteresis loop is established using the stress amplitude of 450 MPa approximately after seven loading cycles. Four loading cycles are necessary to produce a stable hysteresis curve using the stress amplitude of 500 MPa. Overall one hundred loading cycles were simulated.

Ten load cycles of the moving Hertz pressure distribution over a rail part are performed assuming a full slip case. The maximum of the Hertz pressure distribution is set to 800 MPa. The results are shown in Fig. 12.

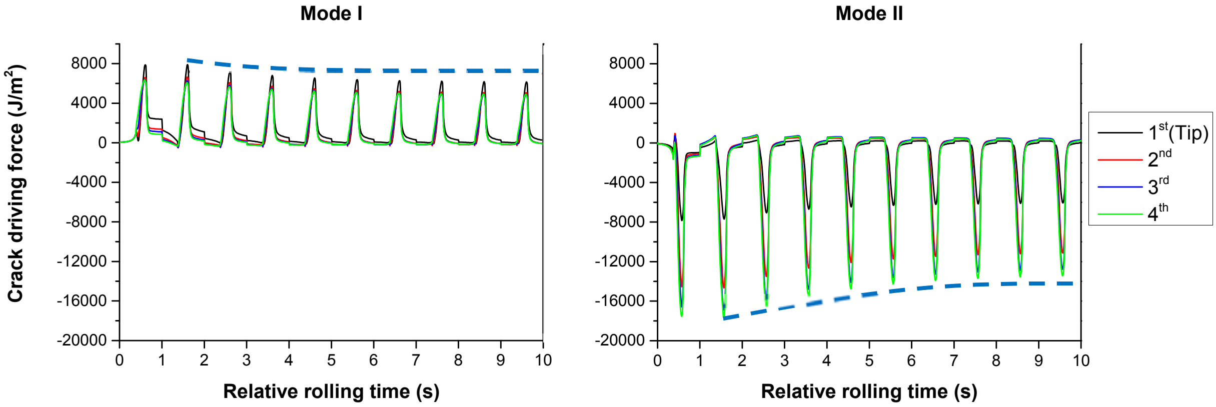

a) b)

Fig. 12: The crack driving force is plotted for ten load cycles rolling with a moving Hertz pressure and a maximum contact pressure of 800 MPa in a full slip case and frictionless contact between the crack faces for Mode I (a) and Mode II (b). The dashed lines mark the stabilisation of the computed crack driving force after about 10 rolling cycles. Constant values are achieved in the 9th rolling cycle for the given loading and material properties. One load pass is performed per second.

The computed crack driving forces show in nearly all cases similar values after the 9th rolling cycle for the given loading and the used material properties. The highest changes of the crack driving force are visible in the first three loading cycles, see Fig. 12. The highest change of the crack driving force corresponds with the ratcheting behaviour observed in the first cycles of the cyclic compression/tensile single element test, see Fig. 11. This observation follows the statement that the bulk configurational force is proportional to the gradient of the plastic strain (in context of the incremental theory of plasticity) as (34):

$$f^{ep} = \sigma \cdot \frac{\partial e_p}{\partial X}, \tag{11}$$

where σ is the Cauchy stress tensor and $\partial e_p / \partial X$ is the gradient of the plastic strain respecting the reference configuration.

A stabilized crack driving force after a certain number of cycles, which are still numerically affordable, is a prerequisite to predict a crack growth rate in further cycles (the crack growth rate calculations have been already presented in (25)).

CONCLUSIONS

The crack driving forces for surface cracks under rolling sliding wheel/rail contact are calculated based on the configurational force concept. The investigations use a 2-D FE crack model to describe the wheel/rail contact situation. Two model variants that represent the contact load are compared: A moving Hertz pressure and a modelled wheel part which is rolling/sliding along the rail part. The investigations reveal differences in the computed crack driving forces between the two models because of the interaction of the crack with the contacting wheel. Some basic variations for investigating e.g. mesh dependence of the FE model, influence of the contact pressure and wheel/rail as well as crack face friction are carried out using linear-elastic material properties. The crack driving forces for Mode II exhibit a dependency on the integration contour even in the case of a frictionless contact between the crack faces. The friction coefficient between the crack faces reduces in all investigated cases the computed crack driving force, on the other hand the wheel/rail friction increases the computed crack driving forces. A higher contact pressure produces a higher crack driving force in Mode II while crack driving forces for Mode I are practically unaffected.

The effect of the plastic deformation on the computed crack forces is investigated using a Chaboche (combined isotropic-kinematic hardening) material model of rail grade R260. The crack driving force is path dependent when the plastic deformation due to the rolling/sliding contact intersects the area enclosed by the integration contours.

The following are concluded from the investigations:

- the contact loading should be applied through a rolling/sliding wheel part rather than by moving Hertz pressure distribution,
- it is reasonable to evaluate the computed crack driving force at the crack tip,

- if a crack is introduced in a model with elastic-plastic material behaviour, it needs ten cycles to reach a steady state around the crack but a steady state is dependent on the underlying material model. From them (ten cycles) a stable crack driving force can be assumed for all further cycles.

REFERENCES

(1) Huang, Y. B.; Shi, L. B.; Zhao, X. J.; Cai, Z. B.; Liu, Q. Y.; Wang, W. J. On the formation and damage mechanism of rolling contact fatigue surface cracks of wheel/rail under the dry condition. Wear 2018, 400-401, 62-73, ISSN 0043-1648.

(2) Jun, H.-K.; Lee, D.-H.; Kim, D.-S. Calculation of minimum crack size for growth under rolling contact between wheel and rail. Wear 2015, 344-345, 46-57, ISSN 0043-1648.

(3) Daves, W.; Kráčalík, M. Cracks Loaded by Rolling Contact - Influence of Plasticity around the Crack. Materials Structure & Micromechanics of Fracture VIII, Jan 2017; pp 221-224, ISSN 1662-9779

(4) Daves, W.; Kubin, W.; Scheriau, S.; Pletz, M. A finite element model to simulate the physical mechanisms of wear and crack initiation in wheel/rail contact. Wear 2016, 366-367, 78-83, Contact Mechanics and Wear of Rail / Wheel Systems, CM2015, August 2015, ISSN 0043-1648.

(5) Kubin, W. K.; Pletz, M.; Daves, W.; Scheriau, S. A new roughness parameter to evaluate the near-surface deformation in dry rolling/sliding contact. Tribology International 2013, 67, 132-139, ISSN 0301-679X.

(6) Caprioli, S. Short rolling contact fatigue and thermal cracks under frictional rolling – A comparison through simulations. Engineering Fracture Mechanics 2015, 141, 260-273, ISSN 0013-7944.

(7) Walia, M. S.; Esmaeili, A.; Vernersson, T.; Lundén, R. Thermomechanical capacity of wheel treads at stop braking: A parametric study. International Journal of Fatigue 2018, 113, 407-415, ISSN 0142-1123.

(8) Hardwick, C.; Lewis, R.; Eadie, D. T. Wheel and rail wear—Understanding the effects of water and grease. Wear 2014, 314, 198-204, Proceedings of the 9th International Conference on Contact Mechanics and Wear of Rail / Wheel Systems, Chengdu, 2012, ISSN 0043-1648.

(9) Wang, W. J.; Lewis, R.; Yang, B.; Guo, L. C.; Liu, Q. Y.; Zhu, M. H. Wear and damage transitions of wheel and rail materials under various contact conditions. Wear 2016, 362-363, 146-152, ISSN 0043-1648.

(10) Vo, K. D.; Zhu, H. T.; Tieu, A. K.; Kosasih, P. B. Comparisons of stress, heat and wear generated by AC versus DC locomotives under diverse operational conditions. Wear 2015, 328-329, 186-196, ISSN 0043-1648.

(11) Fletcher, D. I. Numerical simulation of near surface rail cracks subject to thermal contact stress. Wear 2014, 314, 96-103, Proceedings of the 9th International Conference on Contact Mechanics and Wear of Rail / Wheel Systems, Chengdu, 2012, ISSN 0043-1648.

(12) Cannon, D. F.; Pradier, H. Rail rolling contact fatigue Research by the European Rail Research Institute. Wear 1996, 191, 1-13, 4th International Conference on Contact Mechanics and Wear of Rail-Wheel Systems, ISSN 0043-1648.

(13) Bogdanski, S.; Olzak, M.; Stupnicki, J. Numerical stress analysis of rail rolling contact fatigue cracks. Wear 1996, 191, 14-24, 4th International Conference on Contact Mechanics and Wear of Rail-Wheel Systems, ISSN 0043-1648.

(14) Seo, J.; Kwon, S.; Jun, H.; Lee, D. Fatigue crack growth behavior of surface crack in rails. Procedia Engineering 2010, 2, 865-872, ISSN 1877-7058.

(15) Seo, J.-W.; Kwon, S.-J.; Lee, D.-H.; Choi, H.-Y. Analysis of contact fatigue crack growth using twin-disc tests and numerical evaluations. International Journal of Fatigue 2013, 55, 54-63, ISSN 0142-1123.

(16) Benuzzi, D.; Bormetti, E.; Donzella, G. Stress intensity factor range and propagation mode of surface cracks under rolling–sliding contact. Theoretical and Applied Fracture Mechanics 2003, 40, 55-74, ISSN 0167-8442.

(17) Brouzoulis, J. Wear impact on rolling contact fatigue crack growth in rails. Wear 2014, 314, 13-19, Proceedings of the 9th International Conference on Contact Mechanics and Wear of Rail / Wheel Systems, Chengdu, 2012, ISSN 0043-1648.

(18) Brouzoulis, J.; Ekh, M. Crack propagation in rails under rolling contact fatigue loading conditions based on material forces. International Journal of Fatigue 2012, 45, 98-105, ISSN 0142-1123.

(19) Larijani, N.; Brouzoulis, J.; Schilke, M.; Ekh, M. The effect of anisotropy on crack propagation in pearlitic rail steel. Wear 2014, 314, 57-68, Proceedings of the 9th International Conference on Contact Mechanics and Wear of Rail / Wheel Systems, Chengdu, 2012, ISSN 0043-1648.

(20) Fischer, F. D.; Daves, W.; Pippan, R.; Pointner, P. Some comments on surface cracks in rails. Fatigue & Fracture of Engineering Materials & Structures 2006, 29, 938-948, ISSN 1460-2695.

(21) Trollé, B.; Baietto, M.-C.; Gravouil, A.; Mai, S. H.; Prabel, B. 2D fatigue crack propagation in rails taking into account actual plastic stresses. Engineering Fracture Mechanics 2014, 123, 163-181, Multiaxial Fracture 2013, ISSN 0013-7944.

(22) Pletz, M.; Daves, W.; Yao, W.; Kubin, W.; Scheriau, S. Multi-scale finite element modeling to describe rolling contact fatigue in a wheel–rail test rig. Tribology International 2014, 80, 147-155, ISSN 0301-679X.

(23) Pletz, M.; Daves, W.; Yao, W.; Ossberger, H. Rolling contact fatigue of three crossing nose materials—Multiscale FE approach. Wear 2014, 314, 69-77, Proceedings of the 9th International Conference on Contact Mechanics and Wear of Rail / Wheel Systems, Chengdu, 2012, ISSN 0043-1648.

(24) Kráčalík, M.; Trummer, G.; Daves, W. Application of 2D finite element analysis to compare cracking behaviour in twin-disc tests and full scale wheel/rail experiments. Wear 2016, 346-347, 140-147, ISSN 0043-1648.

(25) Daves, W.; Kráčalík, M.; Scheriau, S. Analysis of crack growth under rolling-sliding contact. International Journal of Fatigue 2019, 121, 63-72, ISSN 0142-1123.

(26) Bogdański, S.; Brown, M. W. Modelling the three-dimensional behaviour of shallow rolling contact fatigue cracks in rails. Wear 2002, 253, 17-25, CM2000 S.I., ISSN 0043-1648.

(27) Mai, S. H.; Gravouil, A.; Nguyen-Tajan, M. L.; Trollé, B. Numerical simulation of rolling contact fatigue crack growth in rails with the rail bending and the frictional contact. Engineering Fracture Mechanics 2017, 174, 196-206, Special Issue on Multiaxial Fracture 2016, ISSN 0013-7944.

(28) Nejad, R. M.; Shariati, M.; Farhangdoost, K. Effect of wear on rolling contact fatigue crack growth in rails. Tribology International 2016, 94, 118-125, ISSN 0301-679X.

(29) Kráčalík, M.; Daves, W.; Antretter, T. Calculation of crack driving forces of surface cracks subjected to rolling/sliding contact. Engineering Fracture Mechanics 2016, 152, 10-25, ISSN 0013-7944.

(30) Kráčalík, M. Influence of the vehicle-track parameters on the crack growth in rails; Ph.D. dissertation; Montauniversität Leoben, 2015.

(31) Ochensberger, W.; Kolednik, O. Physically appropriate characterization of fatigue crack propagation rate in elastic-plastic materials using the J-integral concept. International Journal of Fracture 2015, 192, 25-45, ISSN: 1573-2673.
(32) Simha, N. K.; Fischer, F. D.; Shan, G. X.; Chen, C. R.; Kolednik, O. J-integral and crack driving force in elastic–plastic materials. Journal of the Mechanics and Physics of Solids 2008, 56, 2876-2895, ISSN: 0022-5096.
(33) Kolednik, O.; Predan, J.; Fischer, F. D. Reprint of "Cracks in inhomogeneous materials: Comprehensive assessment using the configurational forces concept". Engineering Fracture Mechanics 2010, 77, 3611-3624, Computational Mechanics in Fracture and Damage: A Special Issue in Honor of Prof. Gross., ISSN 0013-7944.
(34) Kolednik, O.; Schöngrundner, R.; Fischer, F. D. A new view on J-integrals in elastic-plastic materials. International Journal of Fracture 2014, 187, 77-107, ISSN 1573-2673.
(35) Mueller, R.; Kolling, S.; Gross, D. On configurational forces in the context of the finite element method. International Journal for Numerical Methods in Engineering 2002, 53, 1557-1574 ISSN 1097-0207.
(36) Mueller, R.; Gross, D.; Maugin, G. A. Use of material forces in adaptive finite element methods. Computational Mechanics 2004, 33, 421-434, ISSN 0178-7675.
(37) Rice, J. R. A Path Independent Integral and the Approximate Analysis of Strain Concentration by Notches and Cracks. Journal of Applied Mechanics 1968, 35, 379-385, ISSN 0021-8936.
(38) Ochensberger, W.; Kolednik, O. A new basis for the application of the J-integral for cyclically loaded cracks in elastic-plastic materials. International Journal of Fracture 2014, 189, 77-101, ISSN 1573-2673.